ADVANCED MATERIALS
www.advmat.de

Picometer-Level In Situ Manipulation of Ferroelectric Polarization in Van der Waals layered InSe

Hanbin Gao, Ziyuan Liu, Yue Gong, Changming Ke,* Ning Guo, Juanxia Wu, Xin Zeng, Jianfeng Guo, Songyang Li, Zhihai Cheng, Jiawei Li, Hongwei Zhu, Li-Zhi Zhang, Xinfeng Liu, Shi Liu, Liming Xie,* and Qiang Zheng**

Ferroelectric 2D van der Waals (vdW) layered materials are attracting increasing attention due to their potential applications in next-generation nanoelectronics and in-memory computing with polarization-dependent functionalities. Despite the critical role of polarization in governing ferroelectricity behaviors, its origin and relation with local structures in 2D vdW layered materials have not been fully elucidated so far. Here, intralayer sliding of approximately six degrees within each quadruple-layer of the prototype 2D vdW ferroelectrics InSe is directly observed and manipulated using sub-angstrom resolution imaging and in situ biasing in an aberration-corrected scanning transmission electron microscope. The in situ electric manipulation further indicates that the reversal of intralayer sliding can be achieved by altering the electric field direction. Density functional theory calculations reveal that the reversible picometer-level intralayer sliding is responsible for switchable out-of-plane polarization. The observation and manipulation of intralayer sliding demonstrate the structural origin of ferroelectricity in InSe and establish a dynamic structural variation model for future investigations on more 2D ferroelectric materials.

1. Introduction

Owing to the non-coincidence of positive and negative charge centers in a unit cell, ferroelectric materials emerge spontaneous electric polarization and can be utilized in the field of logic computation, data storage photogalvanic effect, etc.[1–2] Recently, ferroelectricity has been discovered in 2D van der Waals (2D vdW) layered materials,[3,4] which yield a wealth of potential applications, such as in memory computing, and efficient ferroelectric photovoltaics, due to the electric-field switchable polarization and the distinctive electronic band structures.[5–8] However, owing to special intralayer structures and weak bonding between van der Waals layers, the origin of ferroelectricity in 2D vdW materials is still not completely explicit, which thereby has been attracting intense attention. In some 2D vdW layered materials with intrinsic ferroelectricity, such as $CuInP_2S_6$,[3,9] In_2Se_3,[10–14] and IV–VI group compounds (SnTe,[4] SnSe,[15] and SnS[16,17]), it has been identified that the spontaneous electric polarization originates from the non-centrosymmetry in each monolayer in their structures. In addition, it's worth mentioning that interlayer slides can easily occur between neighboring layers in 2D vdW layered materials, due to their weak vdW interactions,

H. Gao, Y. Gong, N. Guo, J. Wu, X. Zeng, X. Liu, L. Xie, Q. Zheng
CAS Key Laboratory of Standardization and Measurement for Nanotechnology
National Center for Nanoscience and Technology
Beijing 100190, China
E-mail: gongy@nanoctr.cn; xielm@nanoctr.cn; zhengq@nanoctr.cn

Z. Liu, L.-Z. Zhang
Laboratory of Theoretical and Computational Nanoscience
National Center for Nanoscience and Technology
Beijing 100190, China

C. Ke, S. Liu
Department of Physics
School of Science and Research Center for Industries of the Future
Westlake University
Hangzhou, Zhejiang 310030, China
E-mail: kechangming@westlake.edu.cn

The ORCID identification number(s) for the author(s) of this article can be found under https://doi.org/10.1002/adma.202404628

DOI: 10.1002/adma.202404628

C. Ke, S. Liu
Institute of Natural Sciences
Westlake Institute for Advanced Study
Hangzhou, Zhejiang 310024, China

J. Guo
Institute of Physics
Chinese Academy of Sciences
Beijing 100190, China

S. Li, Z. Cheng
Key Laboratory of Quantum State Construction and Manipulation (Ministry of Education)
Department of Physics
Renmin University of China
Beijing 100872, China

J. Li, H. Zhu
School of Materials Science and Engineering
Tsinghua University
Beijing 100190, China

X. Liu, L. Xie, Q. Zheng
University of Chinese Academy of Sciences
Beijing 100049, P. R. China

which may cause breaking of centrosymmetry and induce sliding ferroelectricity.[18–21]

Notably, 2D vdW layered InSe, with high mobility ($\approx 10^3$ cm^2 V^{-1} s^{-1})[22] and tunable direct bandgap,[23–25] have been studied for in-memory computing and achieved long retention time, high program/erase ratios, and stable cyclic endurance. For instance, three layers-thick InSe field-effect transistor (FET) can realize recording high transconductance of 6 mS μm^{-1} and a room-temperature ballistic ratio of 83% in the saturation region, demonstrating for the first time that 2D FETs are able to deliver actual performance close to that of theoretical prediction and are strong competitors for silicon-based FETs at the angstrom-level node.[26] The bulk InSe consists of 2D vdW-bonding stacked Se–In–In–Se quadruple-layers (QLs) and mainly owns three different structures and phases. According to the stacking configurations of QLs, InSe can be divided into β-InSe (AA′AA′...), ϵ-InSe (ABAB...), and γ-InSe (ABCABC...) phases. Recently, the coexistence of in-plane and out-of-plane ferroelectricity was discovered experimentally in 7 nm thick β-InSe flakes, as well as the effect of its polarization on the drain current characteristics.[27,28] Moreover, γ-InSe was theoretically predicted to exhibit spontaneous polarization and sliding ferroelectricity.[29] However, few experimental investigations have been performed to clarify the origin of their ferroelectricity, other than the recent work on the spontaneous polarization induced by Se displacements[30] and the interlayer sliding ferroelectricity in γ-InSe triggered by yttrium doping (InSe: Y).[31] Therefore, it is highly required to probe into the structural origin of ferroelectricity in InSe, especially the relation between polarization and local structures, based on real-time direct observations of variation of InSe structures and the corresponding ferroelectricity.

In this work, we combine in situ electric manipulation with atomic-scale aberration-correction scanning transmission electron microscopy (STEM) tools to investigate the structure variation of γ-InSe under variable external electric fields in real space. We directly visualize and quantify the picometer-level intralayer sliding of the Se and In sublayers within each quadruple-layer (QL), which breaks the mirror symmetry of monolayer structure and induces alignment of dipole moments and ferroelectricity, thereby suggesting the presence of monolayer ferroelectricity. Meanwhile, the intralayer sliding and the resultant ferroelectric polarization can be manipulated and controlled at the atomic scale through different external electric fields. The unique intralayer sliding within each QL monolayer in InSe is distinct from interlayer sliding commonly observed in many other 2D ferroelectrics. This work reflects that the manner of intralayer sliding is one important origin of ferroelectricity in 2D materials, and also provides valuable insight into the potential applications of 2D vdW ferroelectric materials in electric-field-controlled devices.

2. Results and Discussion

Bulk InSe material was chosen for focused ion beam (FIB) fabrication in our in situ investigations. Powder X-ray diffraction (XRD) results show the sample consists of both γ-phase and ϵ-phase (Figure S1, Supporting Information), in agreement with the previous work.[30] In the γ-phase, In and Se atoms are bonded in the Se–In–In–Se QLs, which stack in the ABC sequence. The structure model of γ-InSe and the definition of short and long In—Se bonds within each QL are shown in **Figure 1a**. By means of optical microscopy and scanning electron microscopy (SEM) imaging, the layered structure both in the millimeter scale and the micron scale was confirmed in our sample (Figure S2, Supporting Information). Energy dispersive X-ray spectroscopy (EDS) element mapping of InSe shows the uniform distribution of the In and Se elements (Figure S3, Supporting Information).

To explore the structural variation of InSe under external electric fields, we used an electrochemically etched tungsten tip to apply different electric fields on a FIB fabricated InSe specimen in an aberration-corrected scanning transmission electron microscope. Figure 1b displays a low-magnification high-angle annular dark-field STEM (HAADF-STEM) image and the schematic of the InSe specimen with Pt capping layers and the tungsten tip. To avoid the occurrence of the short-circuit, the connection between the Pt deposition layers and bilateral thick regions was cut off by FIB, showing the distance affected by external electric fields along the out-of-plane direction is ≈2–3 μm. In order to well visualize the two types of elements simultaneously and improve the contrast of lighter Se atoms, atomic-resolution integrated differential phase contrast (iDPC) imaging, which can reveal intensities roughly proportional to Z (Z is the atomic number), was employed to record local structure variation under different electric fields and investigate the origin of electric field-induced polarization in InSe.

Figure 1c shows a typical iDPC-STEM image of pristine InSe along the [010] direction without biasing. The inset fast Fourier transform (FFT) pattern of this iDPC image reveals that all visible reflections follow the reflection conditions of the *R3m* space group for the γ-phase. Through the quantitative analysis of the positions of all atomic columns obtained by 2D Gaussian fitting, we find that the Se atoms in each QL slightly displace from the symmetric positions. Figure 1d,e exhibits displacement vectors of Se atoms and the corresponding schematic. Such Se displacements can also be reflected by quantified angles between In—Se bonds and the horizontal -In-In- line (α_1 and α_2) (Figure 1e) and In–Se distances in each QL. As shown in Figure 1f, each horizontal -In-In- line was fitted linearly so that angles between In—Se bonds and this line (α_1 and α_2) could be calculated, revealing an obvious difference between α_1 and α_2, which actually should be identical in the ideal perfect γ-phase structure. Furthermore, two kinds of In–Se distances were calculated, indicating the long In–Se distances in the upper In–Se layer are longer than those in the lower In–Se layer in each QL, while the corresponding short In–Se distances show no obvious difference (Figure 1f). Meanwhile, another type of spontaneous polarization domain (Figure S4, Supporting Information) can also be observed in InSe, in which Se displaces toward opposite directions as compared to these in the domain in Figure 1c–f. No spontaneous interlayer sliding could be observed. These results are consistent with our previous work on the spontaneous polarization in InSe.[30]

Second-harmonic generation (SHG) and piezoresponse force microscopy (PFM) measurements were also performed to understand the bulk ferroelectric of γ-InSe. 2D γ-InSe belongs to C_{3v}^5 space group, which possesses noncentral symmetry. SHG measurements are carried out at room temperature in a reflection geometry, as shown in Figure S5a (Supporting Information).

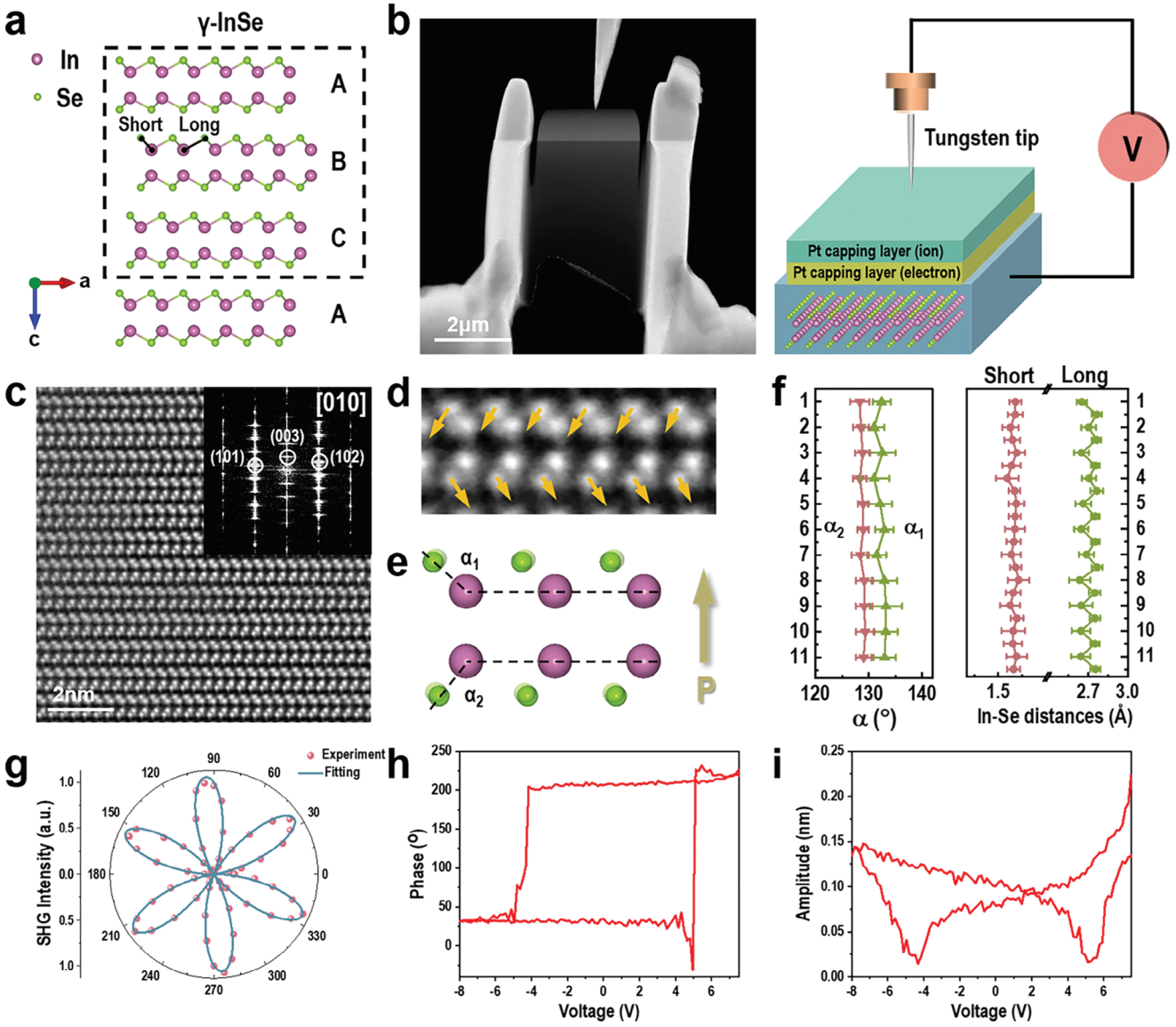

Figure 1. In situ electric experiment setup and spontaneous ferroelectric structure in InSe. a) Crystal structure model of InSe. b) STEM image and corresponding schematic of in situ biasing setup. c) iDPC image of pristine InSe along the [010] direction. The inset shows the corresponding FFT pattern. Displacement vectors for Se atoms and the corresponding structure model with the angles between the In—Se bond and horizontal -In-In- line (α_1 and α_2) are shown in d,e), respectively. f) Quantified average α_1, α_2, short and long In–Se distances for each Se–In–In–Se QL in (c), indicate the spontaneous ferroelectric polarization in pristine InSe is due to picometer-level displacement of Se. g) SHG intensities as a function of the detection angle under the perpendicular polarization configuration. h,i) The local PFM phase hysteresis loops and amplitude during the switching process of the γ-InSe flake after revoking the electric field (OFF mode).

The wavelength of excitation source is 1030 nm, and a signal at 515 nm is collected. Polarization-dependent SHG signals are collected by rotating the sample from 0° to 360° along the anticlockwise direction, where the angle of 0° is the direction of sample placement before SHG measurement, which is shown in the optical image of the sample in Figure S5b (Supporting Information). For this thin γ-InSe sheet, the obvious six-petal patterns are observed under both parallel (Figure S5c, Supporting Information) and cross (Figure 1g) polarization configuration, indicating the threefold rotational symmetry, which is consistent with previous work of SHG property of γ-InSe.[32–35] The armchair and zigzag lattice directions can be easily distinguished, demonstrating that γ-InSe behaves the anisotropy with broken inversion symmetry and directional selectivity. Similar polarization dependence can be observed in different γ-InSe samples with different thicknesses, explaining that the broken spatial inversion symmetry is not induced by the coincidence of positive and negative charge centers.[31] Further electric field modulated SHG measurement (Note Text S1 and Figure S6, Supporting Information) reveals SHG intensity was enhanced by the electric field, suggesting that the polarization of γ-InSe can be manipulated by applying an external electric field.

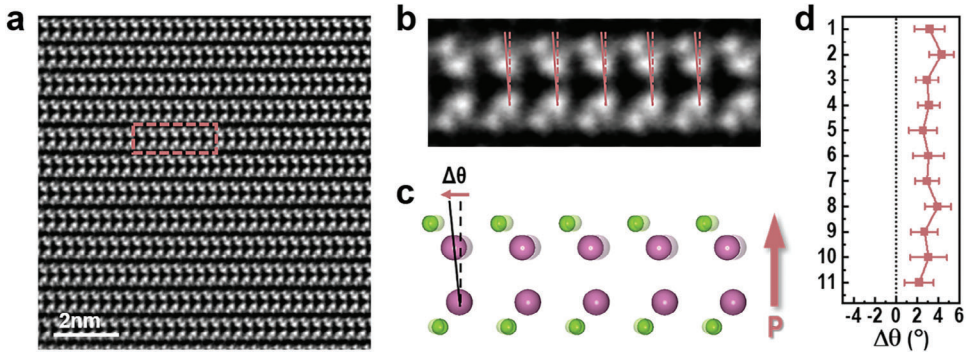

Figure 2. Picometer-level displacement under an upward electric field in InSe. a) iDPC image of InSe along the [010] direction under a voltage of +35 V. b) Magnified image of the pink rectangle region in (a) shows the upper Se–In layer slides toward left, i.e., [$\bar{1}$00] direction, relative to the lower In–Se layer. c) Corresponding intralayer slide model. d) Average slide angles ($\Delta\theta$) between the upper Se–In layer and lower In–Se layer for each Se–In–In–Se QL in (a).

PFM measurements were conducted on γ-InSe sheets using atomic force microscopes in the dual amplitude resonance tracking (DART) mode to investigate the ferroelectric properties. The PFM amplitude and phase hysteresis loops after revoking the electric field (OFF mode) (Figure 1h,i) are obtained at an individual point on γ-InSe sample (see optical and AFM images in Figure S7, Supporting Information) with voltage-swept from −10 to +10 V. A obvious butterfly-shape amplitude curve with hysteresis can be observed. At the same time, the phase switches from 30° to 210° at the same turning point. The phenomena in amplitude and phase hysteresis loops indicate the robust ferroelectricity of γ-InSe sample, distinct from piezoelectric effects. The amplitude and phase hysteresis loops remain the same shapes after 3 cycles of testing, indicating the stability of the ferroelectricity of the γ-InSe sample.

To probe into the atomic-scale origin of ferroelectricity of InSe under external electric fields, in situ biasing STEM experiments were thereby carried out. By moving the W-tip to contact the FIB fabricated InSe specimen, an external electric field can be applied to it. To begin with, we applied a positive bias on the sample, which was increased from 0 to +35 V with 1 V step per second. Each external field was held for two minutes to maximize its effect on the local structure of the specimen,[36] and then W-tip was retracted to enhance the stability of the in situ holder. A series of iDPC images at different voltages were obtained, as an iDPC image for the applied voltage of +35 V exemplified in **Figure** 2a. Positions of In and Se atoms in each iDPC image were obtained by 2D Gaussian fits. Surprisingly, quite different from Se displacements in QL under zero field, an intralayer slide between two In layers in each QL could be observed, after the specimen was experienced an applied voltage of +35 V, as reflected by the slide angles ($\Delta\theta$) between two In layers in each QL deviating from the ideal perfect positions in Figure 2b. $\Delta\theta$ were calculated by subtracting 90° from the values of angles between In—In bonds and the horizontal -In-In- line, and the average value of $\Delta\theta$ for all QLs in Figure 2a is ≈3.08°, revealing the upper Se–In layer in each QL slides slightly along the [$\bar{1}$00] directions relative to the lower In–Se layer (Figure 2c,d). iDPC image was also acquired for an external electric field at an intermediate voltage of +20 V, however, no significant change for $\Delta\theta$ could be reflected (Figure S8, Supporting Information), probably due to the much smaller intralayer slide at this voltage. This type of local structure distortion can break the inversion symmetry in the monolayer and result in intralayer polarization.

Subsequently, we altered the external electric field to −35 V with 1 V step per second and acquired a series of iDPC images at the same conditions as the above positive bias experiment. As shown in a typical iDPC image for the voltage of −35 V in **Figure** 3a,b, the intralayer polarization reversal occurred at this negative voltage, as compared to the positive bias. The slide angles ($\Delta\theta$) between upper Se–In layers and lower In–Se layers in all QLs are below zero degrees, with an average value of ≈−2.57° (Figure 3b–d), which evidences an opposite distortion direction as compared to that for the positive bias in Figure 2. Consistent with that for the intermediate positive voltage of +20 V, iDPC image for an external electric field at an intermediate voltage of −20 V also reveals no significant change for $\Delta\theta$ (Figure S9, Supporting Information). These direct observations in real-time on the unique reversal of picometer-level intralayer sliding without other obvious structural variation strongly suggest its dominance on polarization flip and ferroelectricity in 2D vdW layered-InSe under electric fields. The degree of local polarization thereby can be reasonably described by the tilting angles within the QL structure unit.

To understand the ferroelectricity observed in QL of InSe, we investigate the polar structures using density functional theory (DFT) based on experimentally acquired data (**Figure** 4). Details of the calculation parameters can be found in the Experimental Section. We confirm the polarization reversal induced by the change in the tilting angle ($\Delta\theta$), consistent with experimental observations. The polarization induced by charge transfer changes linearly with $\Delta\theta$, as shown in Figure 4b. At $\Delta\theta$ = 3°, the out-of-plane (OOP) polarization is −1.0 pC m^{-1}, with a 0.0153 e charge transfer between the upward and downward layers, comparable to the value reported recently in intralayer-slide GaSe.[36] When the electric field changes from +0.0016 to −0.0016 V Å^{-1} in experiments (equivalent to a ±35 V voltage applying on the distance along the out-of-plane direction of 2–3 μm), the value of $\Delta\theta$ changes from 3° to −3°, which corresponds to a change in the potential step from 0.1 to −0.1 eV as computed with DFT (Figure 4c), consistent with the reversal of OOP. Notably, the energy change associated with $\Delta\theta$ = 3° is 0.014 eV per unit cell

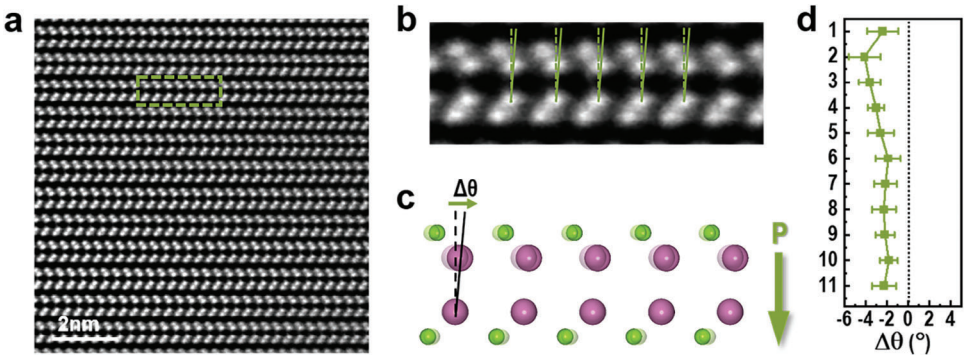

Figure 3. Reversal of picometer-level displacement under downward electric field in InSe. a) iDPC image of InSe along the [010] direction under a voltage of −35 V voltage. b) A magnified image of the green rectangle region in (a) shows the upper In-Se layer slides toward the right, i.e., [100] direction, relative to the lower In–Se layer. c) Corresponding intralayer slide model. d) Quantified average angles ($\Delta\theta$) deviating from symmetrical positions for each Se–In–In–Se QL in (a).

(Figure S10, Supporting Information), which is comparable to energy barriers in many other 2D ferroelectrics. This intralayer sliding may be produced by a built-in electric or strain field in experiments, facilitated by the applied electric field.[37] However, the precise mechanisms behind this phenomenon are still an open question. Moreover, OOP polarization behaviors were also calculated for the two types of spontaneous polarization domains under zero field, of which values are 1.31 and −1.39 pC m^{-1}, respectively. At $\Delta\theta$ = 3°, the in-plane polarization is 2.9 pC m^{-1}, which is three times that of the OOP polarization, as shown in Figure 4b.

Based on the precise in situ electric manipulation of ferroelectric polarization in InSe, the ferroelectricity switching process can be revealed, as depicted in **Figure 5**. The polarization flip is primarily governed by the manner of intralayer sliding within each QL, yet the exact movement of each atomic column is also crucial for understanding the behavior and ferroelectric model of InSe. Hence, in addition to the distances of the Se—In bonds

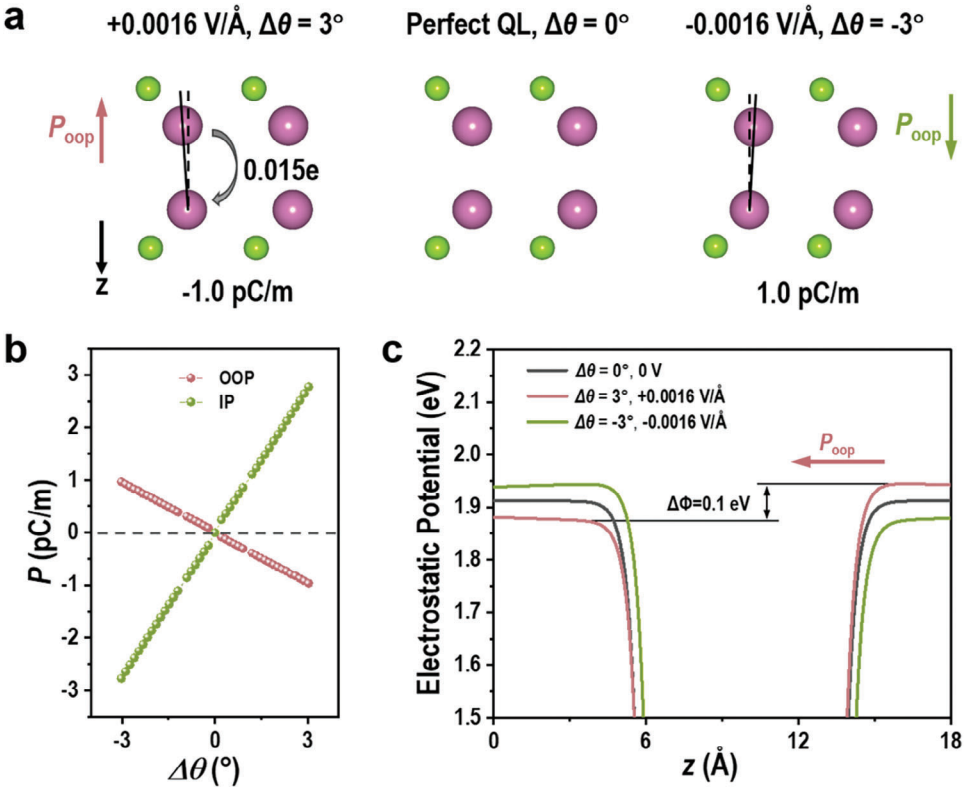

Figure 4. Theoretical calculations on intralayer ferroelectricity in InSe. a) Configuration of the InSe structure with $\Delta\theta$ of 3°, 0°, and −3°. b) Out-of-plane (OOP) and in-plane polarization as functions of tilting angles in the absence of an external electric field. c) Potential step in InSe under applied biases of −35 V (−0.0016 V Å^{-1}), no bias, and +35 V (0.0016 V Å^{-1}).

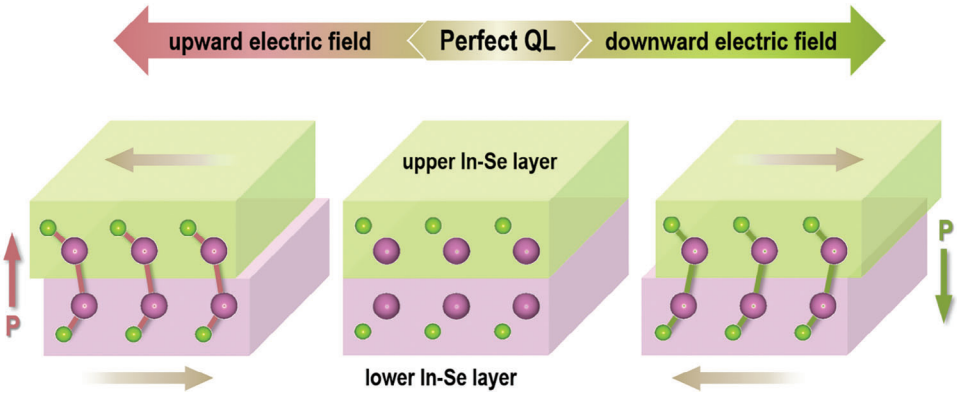

Figure 5. Ferroelectric switching in InSe under various external electric fields. By applying electric fields in opposite directions, the sliding direction of the upper In–Se layer (green cuboid) relative to the lower In–Se layer (purple cuboid) is correspondingly reversed, along with the movement of all In and Se atomic columns.

and sliding angles of $\Delta\theta$ in each QL, we quantified four different angles to describe the relative position variations between In and Se columns, as detailed in Figure S11 and Table S1 (Supporting Information). As shown in Figure 5 and Figure S11 (Supporting Information), in the pristine state, spontaneous ferroelectric polarization is mainly caused by length variations of the two types of In—Se bonds within each QL. With external electric fields of opposite directions applied to InSe, the polarization switching occurs as each Se–In–In–Se unit in QL tilts toward opposite directions within a range of six degrees while distances of the Se—In bond in this unit remain unchanged. Meanwhile, tilting angles of In–Se and In–In within such a unit vary under different electric fields. This suggests that the atoms in each Se–In–In–Se unit move independently, but the polarization direction, which is dictated by the intralayer sliding direction, remains unchanged at each state. Under this circumstance, a simple and clear model can be summarized by considering the QL structure unit as a whole with the sliding angle as a parameter to describe the polarization state of InSe.

3. Conclusion

In summary, through picometer-level quantitative analysis and in situ electric manipulation, we confirm the presence of spontaneous polarization in pristine 2D vdW layered InSe and identify the intralayer sliding ferroelectric switching mechanism, which is modulated by the external electric fields. The angle ($\Delta\theta$), representing the deviation of the upper In–Se layer within each QL from its ideal perfect position, can serve as a critical parameter and indicator to describe the polarization states and levels, which are associated with intralayer sliding-induced ferroelectricity. The observed ferroelectricity in γ-InSe arises intrinsically from intralayer sliding, independent of any doping. This phenomenon, substantiated by experimental data and theoretical calculations, emphasizes the native ferroelectric potential of undoped InSe, which contrasts with the interlayer sliding induced ferroelectricity observed in Y-doped InSe. This work not only establishes the relation between picometer-level structural variation and ferroelectricity but also provides a valuable dynamic model for the investigation and exploration of ferroelectricity in 2D vdW layered materials, paving the way for their various applications in the future.

4. Experimental Section

Synthesis: Bulk InSe crystals were synthesized by the Bridgeman method, in which In powder (99.99%, Alfa) and Se powder (99.99%, Alfa) (molar ratio: 1:1.1) were used as precursors and reacted in a tube furnace at 660 °C for 2 h.

Characterization: Powder X-ray diffraction (XRD) measurements were performed using an X-ray powder diffractometer with Cu K_α radiation (D/MAX-TTRIII(CBO)). The surface morphology of InSe was characterized within a field-emission scanning electron microscope (SU8220, Hitachi), with an energy-dispersive X-ray spectrometer for analysis of elemental distribution and compositions.

STEM specimens were prepared by a focused ion beam (FIB) system (ThermoFisher Scientific, Helios 5 CX). In situ electrical experiments were performed on a double-aberration-corrected transmission electron microscope (Spectra 300, ThermoFisher Scientific), conducted at room temperature (298 K) and operated at 300 kV, with an in situ biasing holder (FE02-DT, Zeptools). Electrochemical etched tip serves as the counter electrode against InSe. High-angle annular dark-field (HAADF)-STEM images were obtained using a probe convergence semi-angle of 25.0 mrad and a collection semi-angle of 62–200 mrad. iDPC images were acquired by a segmented DF4 detector with 4 quadrants. To minimize scan distortion and enhance the signal-to-noise ratio, 15 frames of iDPC-STEM images were acquired sequentially, with a short dwell time of 1 µs px^{-1}. In and Se atomic positions in each iDPC-STEM image were obtained by 2D Gaussian fitting using a custom Matlab code.[38] To ensure STEM observations were universal, more than ten different regions at each electric field were selected for STEM imaging and quantification analysis, all indicating consistent results with those in Figures 1–3, for zero, positive (+35 V), and negative (−35 V) electric fields, respectively. Polarization manner and value were found to remain unchanged during more than 4 h STEM image acquisition process after the removal of each electric field, indicating no obvious polarization decay in at least 4 h after the removal of the electric field.

SHG measurements were performed on a home-made confocal SHG system. A femtosecond laser (Light Conversion) with a central wavelength of ≈1030 nm, pulse light width of ≈190 fs, and repetition frequency of ≈100 kHz was used as excitation source. The Olympus IX73 microscope with a 20× objective was used to focus the laser on the sample and collect the SHG signals in reflection geometry. The laser spot on the sample was ≈3 µm. The laser power of the incident laser on the sample was ≈50 and 150 µW for cross and parallel polarization configuration, respectively. The SHG signals were recorded by the combination of a photon multiplier tube (PMTH-S1 CR131, Zolix) and a lock-in amplifier (SR830 DSP,

Stanford). Cross-polarization configuration was obtained by rotating the polarization direction of the incident laser using a half-wave plate. The polarization-dependent SHG measurements were carried out by rotating the sample from 0° to 360° along the anticlockwise direction. The voltage-modulated SHG measurement was carried out on a home-made SHG system. A mode-locked Ti-sapphire laser was used as the excited light, the central wavelength was 800 nm, and the pulse duration and repetition rate were 120 fs and 80 MHz, respectively. The laser was focused on the γ-InSe sample by a 100× objective lens with N.A. = 0.90, and the laser spot on the sample was ≈3 µm. The SHG signal was back collected using the same lens. The incident beam was separated using a dichroic mirror and further blocked by a 650 nm short-pass filter. The SHG signal was collected using PI Acton 2500i spectrometer with a liquid nitrogen-cooled CCD camera. Moreover, details for electric field modulated SHG measurement are given in Note Text S1 and Figure S6 (Supporting Information).

PFM measurements were conducted on γ-InSe sheets using atomic force microscopes (Oxford-Cypher S; Park-NX10) in the dual amplitude resonance tracking (DART) mode, with conductive Pt-coated Si cantilevers at room temperature under ambient conditions. The PFM amplitude and phase signals were recorded under contact mode.

Theory Calculations: DFT calculations were carried out by using the Vienna ab initio Simulation package[39,40] within the generalized gradient approximation (GGA) of the Perdew–Burke–Ernzerhof (PBE) function.[41] The energy cutoff (ENCUT) of the plane-wave basis was set at 700 eV and the Brillouin zone was sampled by a Gamma-centered *k*-mesh of (12 × 12 × 1). A 30 Å vacuum length along the *z*-direction was set. The tolerance of electronic structure calculations was set to 10^{-7} eV, and the force tolerance for geometric optimization was set at 0.01 eV $Å^{-1}$. Additionally, dipole correction was implemented to account for periodic boundary conditions. The polarization was evaluated by using the Berry-phase method.[42]

Supporting Information

Supporting Information is available from the Wiley Online Library or from the author.

Acknowledgements

H.G. and Z.L. contributed equally to this work. This work was supported by the National Key R&D Program of China (2021YFA1202801 and 2023YFA1406500), the National Natural Science Foundation of China (52172268, 12374176, 52002396, 22105049, 52172046, 61674045, 22475054, and 12304128) and the Strategic Priority Research Program of CAS (XDB36000000). The authors thank Dr. Xiaoyu Li at the Institutional Center for Shared Technologies and Facilities of the Institute of Process Engineering, CAS for the help in the FIB fabrication. The computational resource is provided by Westlake HPC Center. Q.Z. and Y.G. planned and directed the project. H.G., Y.G., and Q.Z. wrote the manuscript and performed the in situ STEM experiment. X.Z., J.W., X.L., and L.X. performed the SHG measurement. S.L., J.G., and Z.C. performed the PFM experiments. H.G. performed data analyses and interpretations with guidance from Y.G. and Q.Z.. C.K., S.L., Z.L., and L-Z.Z. Performed the DFT calculations. J.L. and H.Z. synthesized the InSe sample. All authors commented on the manuscript.

Conflict of Interest

The authors declare no conflict of interest.

Data Availability Statement

The data that support the findings of this study are available from the corresponding author upon reasonable request.

Keywords

aberration-corrected scanning transmission electron microscopy, ferroelectric polarization, in situ electric manipulation, intralayer sliding, van der Waals layered materials

Received: March 30, 2024
Revised: September 26, 2024
Published online:

[1] P. Chen, X. Zhong, J. A. Zorn, M. Li, Y. Sun, A. Y. Abid, C. Ren, Y. Li, X. Li, X. Ma, J. Wang, K. Liu, Z. Xu, C. Tan, L. Chen, P. Gao, X. Bai, *Nat. Commun.* **2020**, *11*, 1840.
[2] X. Li, C. Tan, C. Liu, P. Gao, Y. Sun, P. Chen, M. Li, L. Liao, R. Zhu, J. Wang, Y. Zhao, L. Wang, Z. Xu, K. Liu, X. Zhong, J. Wang, X. Bai, *Proc. Natl. Acad. Sci.* **2020**, *117*, 18954.
[3] F. Liu, L. You, K. L. Seyler, X. Li, P. Yu, J. Lin, X. Wang, J. Zhou, H. Wang, H. He, S. T. Pantelides, W. Zhou, P. Sharma, X. Xu, P. M. Ajayan, J. Wang, Z. Liu, *Nat. Commun.* **2016**, *7*, 12357.
[4] K. Chang, J. Liu, H. Lin, N. Wang, K. Zhao, A. Zhang, F. Jin, Y. Zhong, X. Hu, W. Duan, Q. Zhang, L. Fu, Q.-K. Xue, X. Chen, S.-H. Ji, *Science* **2016**, *353*, 274.
[5] X. Wang, C. Zhu, Y. Deng, R. Duan, J. Chen, Q. Zeng, J. Zhou, Q. Fu, L. You, S. Liu, J. H. Edgar, P. Yu, Z. Liu, *Nat. Commun.* **2021**, *12*, 1109.
[6] S. Wang, L. Liu, L. Gan, H. Chen, X. Hou, Y. Ding, S. Ma, D. W. Zhang, P. Zhou, *Nat. Commun.* **2021**, *12*, 53.
[7] J. Huang, X. Duan, S. Jeon, Y. Kim, J. Zhou, J. Li, S. Liu, *Mater. Horiz.* **2022**, *9*, 1440.
[8] C. Wang, L. You, D. Cobden, J. Wang, *Nat. Mater.* **2023**, *22*, 542.
[9] A. Belianinov, Q. He, A. Dziaugys, P. Maksymovych, E. Eliseev, A. Borisevich, A. Morozovska, J. Banys, Y. Vysochanskii, S. V. Kalinin, *Nano Lett.* **2015**, *15*, 3808.
[10] C. Zheng, L. Yu, L. Zhu, J. L. Collins, D. Kim, Y. Lou, C. Xu, M. Li, Z. Wei, Y. Zhang, M. T. Edmonds, S. Li, J. Seidel, Y. Zhu, J. Z. Liu, W.-X. Tang, M. S. Fuhrer, *Sci. Adv.* **2018**, *4*, eaar7720.
[11] C. Cui, W.-J. Hu, X. Yan, C. Addiego, W. Gao, Y. Wang, Z. Wang, L. Li, Y. Cheng, P. Li, X. Zhang, H. N. Alshareef, T. Wu, W. Zhu, X. Pan, L.-J. Li, *Nano Lett.* **2018**, *18*, 1253.
[12] Y. Zhou, D. Wu, Y. Zhu, Y. Cho, Q. He, X. Yang, K. Herrera, Z. Chu, Y. Han, M. C. Downer, H. Peng, K. Lai, *Nano Lett.* **2017**, *17*, 5508.
[13] W. Ding, J. Zhu, Z. Wang, Y. Gao, D. Xiao, Y. Gu, Z. Zhang, W. Zhu, *Nat. Commun.* **2017**, *8*, 14956.
[14] X. Zheng, W. Han, K. Yang, L. W. Wong, C. S. Tsang, K. H. Lai, F. Zheng, T. Yang, S. P. Lau, T. H. Ly, M. Yang, J. Zhao, *Sci. Adv.* **2022**, *8*, eabo0773.
[15] K. Chang, F. Küster, B. J. Miller, J.-R. Ji, J.-L. Zhang, P. Sessi, S. Barraza-Lopez, S. S. P. Parkin, *Nano Lett.* **2020**, *20*, 6590.
[16] Y. Bao, P. Song, Y. Liu, Z. Chen, M. Zhu, I. Abdelwahab, J. Su, W. Fu, X. Chi, W. Yu, W. Liu, X. Zhao, Q.-H. Xu, M. Yang, K. P. Loh, *Nano Lett.* **2019**, *19*, 5109.
[17] N. Higashitarumizu, H. Kawamoto, C.-J. Lee, B.-H. Lin, F.-H. Chu, I. Yonemori, T. Nishimura, K. Wakabayashi, W.-H. Chang, K. Nagashio, *Nat. Commun.* **2020**, *11*, 2428.
[18] M. Wu, J. Li, *Proc. Natl. Acad. Sci.* **2021**, *118*, e2115703118.
[19] J. Xiao, Y. Wang, H. Wang, C. D. Pemmaraju, S. Wang, P. Muscher, E. J. Sie, C. M. Nyby, T. P. Devereaux, X. Qian, X. Zhang, A. M. Lindenberg, *Nat. Phys.* **2020**, *16*, 1028.
[20] K. Yasuda, X. Wang, K. Watanabe, T. Taniguchi, P. Jarillo-Herrero, *Science* **2021**, *372*, 1458.
[21] M. Vizner Stern, Y. Waschitz, W. Cao, I. Nevo, K. Watanabe, T. Taniguchi, E. Sela, M. Urbakh, O. Hod, M. Ben Shalom, *Science* **2021**, *372*, 1462.

[22] S. Sucharitakul, N. J. Goble, U. R. Kumar, R. Sankar, Z. A. Bogorad, F.-C. Chou, Y.-T. Chen, X. P. A. Gao, *Nano Lett.* **2015**, *15*, 3815.
[23] W. Huang, L. Gan, H. Li, Y. Ma, T. Zhai, *CrystEngComm* **2016**, *18*, 3968.
[24] F. Wu, H. Xia, H. Sun, J. Zhang, F. Gong, Z. Wang, L. Chen, P. Wang, M. Long, X. Wu, J. Wang, W. Ren, X. Chen, W. Lu, W. Hu, *Adv. Funct. Mater.* **2019**, *29*, 1900314.
[25] H. Shang, H. Chen, M. Dai, Y. Hu, F. Gao, H. Yang, B. Xu, S. Zhang, B. Tan, X. Zhang, P. Hu, *Nanoscale Horiz.* **2020**, *5*, 564.
[26] J. Jiang, L. Xu, C. Qiu, L.-M. Peng, *Nature* **2023**, *616*, 470.
[27] H. Hu, Y. Sun, M. Chai, D. Xie, J. Ma, H. Zhu, *Appl. Phys. Lett.* **2019**, *114*, 252903.
[28] H. Hu, H. Wang, Y. Sun, J. Li, J. Wei, D. Xie, H. Zhu, *Nanotechnology* **2021**, *32*, 385202.
[29] M. Wu, *ACS Nano* **2021**, *15*, 9229.
[30] J. Liao, W. Wen, J. Wu, Y. Zhou, S. Hussain, H. Hu, J. Li, A. Liaqat, H. Zhu, L. Jiao, Q. Zheng, L. Xie, *ACS Nano* **2023**, *17*, 6095.
[31] F. Sui, M. Jin, Y. Zhang, R. Qi, Y.-N. Wu, R. Huang, F. Yue, J. Chu, *Nat. Commun.* **2023**, *14*, 36.
[32] Y. Ke, C. Li, Y. Liang, X. Zhang, J. Song, R. Li, L. Liu, J. Dai, Z. Wei, Q. Zhang, *Nanoscale* **2023**, *15*, 10125.
[33] M. Dai, H. Chen, F. Wang, Y. Hu, S. Wei, J. Zhang, Z. Wang, T. Zhai, P. Hu, *ACS Nano* **2019**, *13*, 7291.
[34] Y. Pan, Q. Zhao, F. Gao, M. Dai, W. Gao, T. Zheng, S. Su, J. Li, H. Chen, *ACS Appl. Mater. Interfaces* **2022**, *14*, 21383.
[35] J. Zhou, J. Shi, Q. Zeng, Y. Chen, L. Niu, F. Liu, T. Yu, K. Suenaga, X. Liu, J. Lin, Z. Liu, *2D Mater.* **2018**, *5*, 025019.
[36] W. Li, X. Zhang, J. Yang, S. Zhou, C. Song, P. Cheng, Y.-Q. Zhang, B. Feng, Z. Wang, Y. Lu, K. Wu, L. Chen, *Nat. Commun.* **2023**, *14*, 2757.
[37] Z. Guan, Y.-Z. Zheng, W.-Y. Tong, N. Zhong, Y. Cheng, P.-H. Xiang, R. Huang, B.-B. Chen, Z.-M. Wei, J.-h. Chu, C.-G. Duan, *Adv. Mater.* **2024**, *36*, 2403929.
[38] A. De Backer, K. H. W. van den Bos, W. Van den Broek, J. Sijbers, S. Van Aert, *Ultramicroscopy* **2016**, *171*, 104.
[39] G. Kresse, J. Hafner, *Phys. Rev. B* **1993**, *47*, 558.
[40] G. Kresse, J. Furthmüller, *Comput. Mater. Sci.* **1996**, *6*, 15.
[41] J. P. Perdew, K. Burke, M. Ernzerhof, *Phys. Rev. Lett.* **1996**, *77*, 3865.
[42] R. D. King-Smith, D. Vanderbilt, *Phys. Rev. B* **1993**, *47*, 1651.